

Synthetic spectral structure of the seismic ambient vibrations generated by a distribution of superficial random sources with a finite extension

Enrico Lunedei^{a,*}, Dario Albarello^{b,c}

^a Centro Interdipartimentale "Alma Mater Research Institute on Global Challenges and Climate Change (Alma Climate)", Università degli Studi di Bologna, c/o DIFA, Via Imerio, 46, 40126, Bologna, Italy

^b Dipartimento di Scienze Fisiche, della Terra e dell'Ambiente, Università degli Studi di Siena, Via Laterina 8, 53100, Siena, Italy

^c Istituto di Geologia Ambientale e Geoingegneria, Consiglio Nazionale delle Ricerche, c/o Area della Ricerca di Roma 1, Via Salaria km 29,300, 00015, Montelibretti (Roma), Italy

ARTICLE INFO

Keywords:

Seismic ambient-vibrations
Power spectra
Random wavefield
Correlated loads
HVSr

ABSTRACT

A model of seismic ambient vibrations is presented in the form of a random wavefield generated by a uniform continuous distribution of correlated aleatory forces, located at the surface of a flat layered weakly-dissipative Earth. The frequency-dependent spatial correlation among these sources is assumed to be representative of their spatial extension and has been parametrized by considering the role played by sea-wave dynamics in generating ambient vibrations. This enables a realistic description of the average power spectral density function of ambient vibrations observed worldwide at reference soil conditions. Effectiveness of the model is tested by reproducing observed average Horizontal-to-Vertical Spectral Ratios obtained from ambient vibration measurements at a well documented site in Northern Italy.

1. Introduction

Passive seismic survey is nowadays a widely used technique to infer some mechanical properties of the shallow subsoil, significant in order to characterize the places by means the local seismic effects they manifest. In the last couple of decades, both single-station (e.g., Refs. [1–4]), and multi-station (e.g., Refs. [5–7]), configurations have been used to extract some observables by the ambient-vibration wavefield, which make it possible, by exploiting suitable inversion procedures, to infer the shallow subsoil seismic properties (e.g., Refs. [8,9]).

The use of ambient-vibration measurements to retrieve low-strain seismic properties of the subsoil relies, however, on the development of physical models able to establish a relationship between average properties of this wavefield, measured at the Earth's surface, and the subsoil structure. These forward models, implemented in the inversion procedures, should be characterized by sound physical basis (in that they are able to capture main features of underlying physical processes) and computational effectiveness. These two aspects are in many cases conflicting, since completeness and soundness of the physical model (including, e.g., all the seismic phases expected to contribute to the ambient vibration wavefield) also implies a significant increase of computational efforts necessary to provide realistic outcomes.

In order to maximize computational effectiveness, several simplified forward models have been considered, by assuming as negligible the contribution of some seismic phases. Since array measurements of ambient vibrations focus on the characterization of surface-wave components (see, for a review, Ref. [10]), forward modelling can be performed by considering these phases only. In this case also, some limiting assumptions have to be made and, in particular, that energy partition between the propagation modes only depends on the subsoil structure and not on the generating sources [11,12]. Modelling HVSr curves appears a much more complex task, because, in principle, these curves are expected to depend on the spectral amplitudes of all seismic phases (body and surface waves) present in the ambient vibration wavefield (see, e.g., Ref. [13]). The relative contribution of these different phases is expected to depend on the distribution and characteristics of sources, propagation phenomena and local seismo-stratigraphical conditions. Experimental studies [14,15] and numerical modelling [16] indicate that surface waves (both Rayleigh and Love) dominate some parts of the spectral domain, but other phases may play an important role, in particular in the spectral range below and close to the resonance frequency of the S waves. This implies that simplified models focusing on specific phases only (e.g., Refs. [1,17–19]), may only capture part of the observed phenomenology.

* Corresponding author.

E-mail addresses: enrico.lunedei2@studio.unibo.it (E. Lunedei), dario.albarello@unisi.it (D. Albarello).

<https://doi.org/10.1016/j.soildyn.2021.106949>

Received 29 January 2021; Received in revised form 2 August 2021; Accepted 23 August 2021

Available online 14 September 2021

0267-7261/© 2021 Elsevier Ltd. All rights reserved.

To overcome these problems, full wavefield models have been proposed and applied in the practice of site seismic characterization. An effective model has been proposed by Sánchez-Sesma *et al.* [20] under the simplifying assumption that ambient vibration is a diffuse random wavefield (DFA, Diffuse Field Approach, in the following). This assumption appears appealing, since it allows to remove from the model the role of sources by focusing on the effect that the local structure plays on the ambient vibration spectral structure. Some theoretical consequences of this model have been explored [21] and effective numerical forward computations have been developed and successfully implemented in inversion protocols [22]. The DFA model has proved its effectiveness in many situations (e.g. Refs. [23–26], included the case of offshore measurements [27].

However, disregarding the role of sources cannot allow accounting for observations showing that the shape of the HVSR curve may be, sometimes, affected by the distribution and activity level of ambient vibration sources [28,29].

This suggests that developing a more general model inclusive of ambient vibration sources could be of some interest. Such an alternative model should implement the inherent stochastic nature of the ambient vibrations (cf., e.g., Ref. [30,31]) and the physical description of seismic observations in terms of source characteristics and propagation phenomena. First attempts in this direction were proposed by Field and Jacob [32], Lachet and Bard [53] and Bonnefoy-Claudet *et al.* [33], based on the assumption that ambient vibrations are the effect of a distribution of independent point-like harmonic random sources located at the surface of the Earth. Lunedei and Albarello [34] provided a consistent formalization of that model, by considering a flat layered viscoelastic Earth. In that model, a formal relationship can be established between the average spectral power of the random sources and that of the resulting displacement wavefield at a site. This model allowed to simulate realistic HVSR patterns and also effectively reproduce phase correlations between ambient vibrations measured at multiple sites.

However, the assumption of independent random point sources seems in contrast with the well established oceanic/atmospheric origin of most part of ambient vibrations, at least in the frequency range below 1 Hz [14,35], which implies a finite dimension of the sources. This feature can be described by introducing a form of correlation between the considered point sources and, in particular, the typical dimension (wavelength) of the source can be simulated by imposing a suitable correlation radius. A first attempt in this direction has been provided in Lunedei and Albarello [36] by considering a correlation radius whose dimension is independent from the vibration periods of point-like sources. This model, however, seems to be unrealistic since it is plausible that source dimensions may affect the range of excited frequencies. Specifically, oceanic swells, most probably responsible for observed ambient vibrations in the low-frequency range, are characterized by a well defined relationship between wavelength λ and frequency ν in the approximate form

$$\lambda = \frac{g}{2\pi} \nu^{-2}, \quad (1)$$

where g is the gravity acceleration modulus [37]. Tanimoto [38] and Webb [39] accounted for this effect at the global scale by modelling ambient vibrations in the very low frequency domain (<0.1 Hz). In order to extend this view to the frequency range of interest for engineering applications (>0.1 Hz), a frequency-dependent correlation radius is introduced in this paper to generalize our previous model [36].

The formalization of the proposed model is presented at first. The tuning of parameters controlling the frequency dependence of the correlation radius is then obtained, by considering as benchmarks Eq. (1) and the shape of average spectral powers defined by Peterson [40] for ambient vibrations measured worldwide at rock sites. Then, a case study is presented, where the effectiveness of the proposed model is evaluated in comparison with observations and outcomes of alternative

formulations.

2. The model

In Lunedei and Albarello [36,41] a model of the ambient-vibration full-wavefield has been proposed in the frame of the Distributed Surface Sources (DSS) hypothesis, in which ambient vibrations are considered as the effect of a distribution of sources located at the surface of the Earth. In this model, the ambient-vibration displacement field,

$$\mathbf{U}(x, y, t) = \begin{pmatrix} U_x(x, y, t) \\ U_y(x, y, t) \\ U_z(x, y, t) \end{pmatrix} \in \mathbb{R}^3,$$

and the field of its generating forces per unit surface (source-tractions),

$$\mathbf{F}(x, y, t) = \begin{pmatrix} F_x(x, y, t) \\ F_y(x, y, t) \\ F_z(x, y, t) \end{pmatrix} \in \mathbb{R}^3,$$

are defined as stochastic fields, being t the time, and $\mathbf{x} \equiv (x, y)^T$ the Cartesian vector describing the position on the Earth's surface. Both these stochastic fields are three-variate, because they have three Cartesian components (the ones of source-stresses and ground-motions), and three-dimensional, because they depend on three variables (the time and the two Cartesian coordinates describing location on the Earth's surface of the sources and of the sites where ground motion is observed), stationary in the time and homogeneous over the Earth's surface (both at least at the second order), with zero mean and finite variance. Moreover, the vertical heterogeneity in the mechanical properties of the subsoil is taken in account only, i.e., the Earth is approximated as a stack of horizontal flat viscoelastic homogeneous and isotropic layers overlying a half-space with analogous properties.

Under the four hypothesis adopted in Lunedei and Albarello [36,41], i.e.,

- 1) displacement stochastic fields linearly depends on the force stochastic fields,
- 2) power spectral density functions exist for both the fields, which are represented by the respective spectral matrices, $\mathbf{h}_U(k_x, k_y, \omega)$ and $\mathbf{h}_F(k_x, k_y, \omega)$,
- 3) the three Cartesian components of the force field are uncorrelated one another, so the force spectral matrix is diagonal, $\mathbf{h}_F(k_x, k_y, \omega) = \text{diag}(h_{F,xx}(k_x, k_y, \omega), h_{F,yy}(k_x, k_y, \omega), h_{F,zz}(k_x, k_y, \omega))$,
- 4) each of the spatial covariances of the three Cartesian components of the force field is isotropic in the horizontal plane,

(see Appendix A for more details) the relationship between the power spectral density functions of the displacement components along the three Cartesian principal directions, $h_{U,ii}$, as a function of the power spectral density functions of source components along the three Cartesian principal directions, $h_{F,ii}$, has been established in the form

$$h_{U,ii}(k, \omega) = \sum_{j=x,y,z} \left| \hat{G}_{ij}(k, \omega) \right|^2 \cdot h_{F,jj}(k, \omega),$$

for all $i = x, y, z$, where ω is the angular frequency, $\mathbf{k} \equiv (k, \varphi)^T$ is the (vectorial) horizontal wavenumber (expressed in a polar coordinate system), $\hat{G}_{ij}(k, \omega)$ are the entries of the Green's matrix in the wavenumber-frequency domain and the functions $h_{F,jj}(k, \omega)$ just depend on the modulus of \mathbf{k} and on the angular frequency ω , as a consequence of the hypothesis of isotropy.

By considering the Fourier-transform relationship between the power spectrum and the spatial-temporal covariance, Lunedei and Albarello [41] express the displacement covariance function between two points located on the horizontal plane (without loss of generality, the first of these points is put in the coordinate origin, while the second is

named \mathbf{x}_0) in the form

$$\mathcal{R}_{U,ii}(\mathbf{x}_0, t) = \frac{1}{(2\pi)^3} \int_{\mathbb{R}^3} h_{U,ii}(\mathbf{k}, \omega) \cdot e^{i(\mathbf{k}\mathbf{x}_0 + \omega t)} d\mathbf{k} d\omega,$$

$i = x, y, z$. Being \mathbf{x}_0 fixed, each of these functions can be viewed as the cross-covariance, with respect the time, between the correspondent component of the displacement at these two receivers. The corresponding cross-spectrum in terms of the relevant temporal Fourier transform is

$$\begin{aligned} p_{U,i}(\mathbf{x}_0, \omega) &\equiv \int_{-\infty}^{+\infty} \mathcal{R}_{U,ii}(\mathbf{x}_0, t) \cdot e^{-i\omega t} dt \\ &= \frac{1}{(2\pi)^2} \sum_{j=x,y,z} \int_{\mathbb{R}^2} \left| \hat{G}_{ij}(\mathbf{k}, \omega) \right|^2 \cdot h_{F,ij}(\mathbf{k}, \omega) \cdot e^{i\mathbf{k}\mathbf{x}_0} d\mathbf{k} \end{aligned} \quad (3)$$

(explicit expressions are reported in Refs. [36,41]. By using this formulation, both surface-wave dispersion curves and HVSR curves can be modeled.

2.1. A new source covariance

Lunedei and Albarello [36] highlight that, in order to provide the convergence of the displacement power integrals in Eq. (3), the source power spectral density functions $h_{F,ij}(\mathbf{k}, \omega)$ must be decreasing as $k \rightarrow +\infty$. As a consequence, the force field representative of surface sources must be “colored”, in that a dependence of force power spectral density function on the wavenumber modulus k is necessary. This kind of dependence also implies the existence of spatial correlation of the source field, which can be physically interpreted as a relationship among point-like sources or as an expression of the source dimension. Indeed, the power spectral density function of each j -th ($j = x, y, z$) direction is the Fourier transform of the relative covariance function $\mathcal{R}_{F,ij}(\mathbf{x}, t)$ (e.g., Refs. [42,43]), viz.

$$h_{F,ij}(\mathbf{k}, \omega) = \int_{\mathbb{R}^3} \mathcal{R}_{F,ij}(\mathbf{x}, t) \cdot e^{-i(\mathbf{k}\mathbf{x} + \omega t)} d\mathbf{x} dt.$$

When expressed in polar coordinates $\mathbf{x} \equiv (r, \theta)^T$ and $\mathbf{k} \equiv (k, \varphi)^T$, isotropy of the force stochastic field means that $\mathcal{R}_{F,ij}$ is just a function of r and t and implies that

$$h_{F,ij}(k, \omega) = 2\pi \cdot \int_{-\infty}^{+\infty} \left\{ \int_0^{+\infty} \mathcal{R}_{F,ij}(r, t) \cdot J_0(kr) \cdot r dr \right\} \cdot e^{-i\omega t} dt,$$

for $j = x, y, z$, where J_0 is the zero-order Bessel function (this expression rectifies Eq. (11) of [36], where the factor 2π is lacking). This formula states that the power-spectral-density dependence on the wavenumber-modulus is expressed by the zero-order Hankel transform with respect to the distance. As the inverse transform has the same structure, it clearly follows that the power spectral density function is isotropic with respect to \mathbf{k} if and only if the covariance function is isotropic with respect to \mathbf{x} . That is, isotropy in the wavenumber-plane of the force power spectral density function implies that the correlation between point-like sources only depends on their reciprocal distance (or that finite-size sources have round shape only), and *vice versa*. It is important to stress that this physically plausible hypothesis does not imply isotropy in the intensity of the source-stress field itself: it can act with different intensities along the three Cartesian directions as well.

In Lunedei and Albarello [36,41] a spatio-temporal separable covariance for the force field has been proposed, in the form

$$\tilde{\mathcal{R}}_{F,ij}(r, t) = \Theta_{F,j}(t) \cdot \frac{b_j}{2\pi d_j^2} \cdot e^{-\frac{r^2}{2d_j^2}}, \quad (4)$$

where b_j and d_j are two positive constants and $\Theta_{F,j}(t)$ is a Fourier-transformable function, for each $j = x, y, z$, which has the remarkable

drawback that its spatial extension is independent of the frequency. In order to overcome this limitation, which is a consequence of the separability hypothesis, a non-separable covariance functions is here introduced in the form

$$\mathcal{R}_{F,ij}(r, t) = \frac{B_j}{\left[\left(\frac{r}{R_j} \right)^2 + 1 \right]^{1/4}} \cdot \exp \left\{ - \frac{\left(\frac{t}{T_j} \right)^2}{4 \sqrt{\left(\frac{r}{R_j} \right)^2 + 1}} \right\}, \quad (5)$$

where $j = x, y, z$ refers to the Cartesian components of the source-tractions acting at the source and B_j , R_j and T_j are positive tuning parameters: B_j represents the variance (spectral intensity) of the random sources wavefield in the j -th direction (in fact, $\mathcal{R}_{F,ij}(0, 0) = B_j$) and the remaining ones determine characteristic space (R_j) and time (T_j) scales for each Cartesian component. This function is everywhere continue and infinitely derivable and fulfils all the constraints requested to a covariance function (see, e.g., Ref. [44]). The source spatial covariance with respect to the frequency is its time Fourier-transform (Appendix B), i.e.,

$$\begin{aligned} C_{F,j}(r; \omega) &= \int_{-\infty}^{+\infty} \mathcal{R}_{F,ij}(r, t) \cdot e^{-i\omega t} dt = \\ &= 2\sqrt{\pi} B_j T_j \cdot \exp \left\{ - (\omega T_j)^2 \sqrt{\left(\frac{r}{R_j} \right)^2 + 1} \right\}, \quad j = x, y, z, \end{aligned} \quad (6)$$

which decays as the distance between the sources increases, in a way depending on the frequency. More precisely, this function is monotonically decreasing with the absolute value of the frequency, i.e., the correlation at each fixed distance $r \geq 0$, is reduced, if the angular frequency is incremented from ω_1 to ω_2 (with $|\omega_2| > |\omega_1|$), by a factor

$$\frac{C_{F,j}(r; \omega_2)}{C_{F,j}(r; \omega_1)} = \exp \left\{ - (\omega_2^2 - \omega_1^2) \cdot T_j^2 \cdot \sqrt{\left(\frac{r}{R_j} \right)^2 + 1} \right\} < 1,$$

for $j = x, y, z$. Being the function $C_{F,j}(r; \omega)$ clearly monotonic both in r and ω , the spatial correlation range gradually reduces as the frequency increases (in modulus). This is a remarkable feature of this correlation model, since it is physically plausible that low-frequency sources are characterized by a spatial correlation (a dimension) more extended than the high-frequency ones.

For each frequency, the correlation between two point sources, separated by an arbitrary distance $r \geq 0$, is given by

$$\text{coh}_{F,j}(r; \omega) = \frac{C_{F,j}(r; \omega)}{C_{F,j}(0; \omega)} = \exp \left\{ - (\omega T_j)^2 \cdot \left[\sqrt{\left(\frac{r}{R_j} \right)^2 + 1} - 1 \right] \right\} \leq 1, \quad (7)$$

for each $j = x, y, z$, which is, by definition, the coherence function of the relative Cartesian component of the source field.

The spatial correlation intensity of the source field can be effectively described, from a physical point of view, by considering a conventional “effective” correlation radius, which is the distance at which the coherence falls below a fixed value $\gamma \in]0, 1$, i.e.,

$$r_{\gamma,j}(\omega) = \frac{R_j \cdot |\log \gamma|}{(\omega T_j)^2} \cdot \sqrt{1 + 2 \frac{(\omega T_j)^2}{|\log \gamma|}} \quad (8)$$

(Appendix B). This effective correlation radius monotonically decreases as the frequency increases (Fig. 1, for $\gamma = 1\%$) and shows, with very good approximation, the same dependence on ω for each parameters-pair for which the ratio R_j/T_j^2 keeps the same value. When this constant is 10 ms^{-2} , the effective radius ranges from about 100 m, at 0.1 Hz, to around 1 m, at 1 Hz, which can be considered as realistic, since roughly

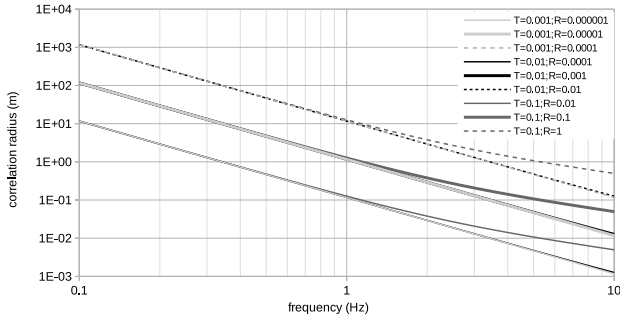


Fig. 1. Force correlation radius for a correlation of 1%. Black, light gray and dark gray refer, respectively, to three values of the time scale parameter T (expressed in seconds). Thick lines refer to parameter-pair linked by Eq. (11), thin continuous lines refer to parameter-pair linked by $R_j/T_j^2 = 1 \text{ ms}^{-2}$, while thin dashed lines refer to parameter-pair linked by $R_j/T_j^2 = 100 \text{ ms}^{-2}$.

corresponds to the typical dimension of sea waves responsible for ambient vibrations. Moreover, $r_{\gamma,j}$ shifts toward higher values if $R_j > (10 \text{ ms}^{-2}) \cdot T_j^2$ and toward lower ones for $R_j < (10 \text{ ms}^{-2}) \cdot T_j^2$, while a clear change in the dependence of $r_{\gamma,j}$ on ω happens when T_j overcomes the value 0.01 s, irrespective of the R_j value. These observations find an easy explanation by taking the zero-order approximation of Eq. (8) for $\omega T_j \ll \sqrt{|\log \gamma|/2}$, i.e.,

$$r_{\gamma,j}(\omega) \simeq \frac{R_j}{T_j^2} \frac{|\log \gamma|}{\omega^2}, \quad (9)$$

and observing that it perfectly mimics Eq. (1), if the effective correlation radius is assumed to be representative of the typical wavelength of the sources. This provides an important constrain for the two scaling

parameters of the correlation function, in the form

$$\frac{R_j}{T_j^2} = \frac{2\pi g}{|\log \gamma|}. \quad (10)$$

When γ is of the order of $10^{-2} \div 10^{-3}$, this relationship implies R_j/T_j^2 values of the order of 10 ms^{-2} , in line with the previous observations. These findings strongly support physical plausibility of the new covariance function in Eq. (5) and suggest that parameter-pair values should fulfill the relationship

$$R_j = 10 \cdot T_j^2, \quad (11)$$

which will be assumed hereafter.

By performing a two-dimensional Fourier transform of $C_{F,j}$ (Eq. (6)) in the spatial variables, the wavenumber–frequency spectral power density function is obtained (Appendix B):

$$\begin{aligned} h_{F,j}(k, \omega) &= 2\pi \int_0^{+\infty} C_{F,j}(r; \omega) \cdot J_0(kr) \cdot r dr = \\ &= \frac{\pi^3 \cdot B_j T_j \cdot (2\omega T_j R_j)^2}{\left[\sqrt{(kR_j)^2 + (\omega T_j)^4} \right]^3} \left[1 + \sqrt{(kR_j)^2 + (\omega T_j)^4} \right] \cdot \\ &\quad \cdot \exp \left\{ -\sqrt{(kR_j)^2 + (\omega T_j)^4} \right\}, \end{aligned} \quad (12)$$

for each $j = x, y, z$. This function is continuous and infinitely derivable everywhere except at the origin $k = \omega = 0$, where it is not defined.

The listed functions are shown in Fig. 2 for $B_j = 1 \text{ Pa}^2$, $T_j = 0.01 \text{ s}$ and $R_j = 0.001 \text{ m}$ ($j = x, y, z$), while the physical dimensions of the involved quantities are discussed in Appendix C.

A final observation concerns the extreme values reached by the

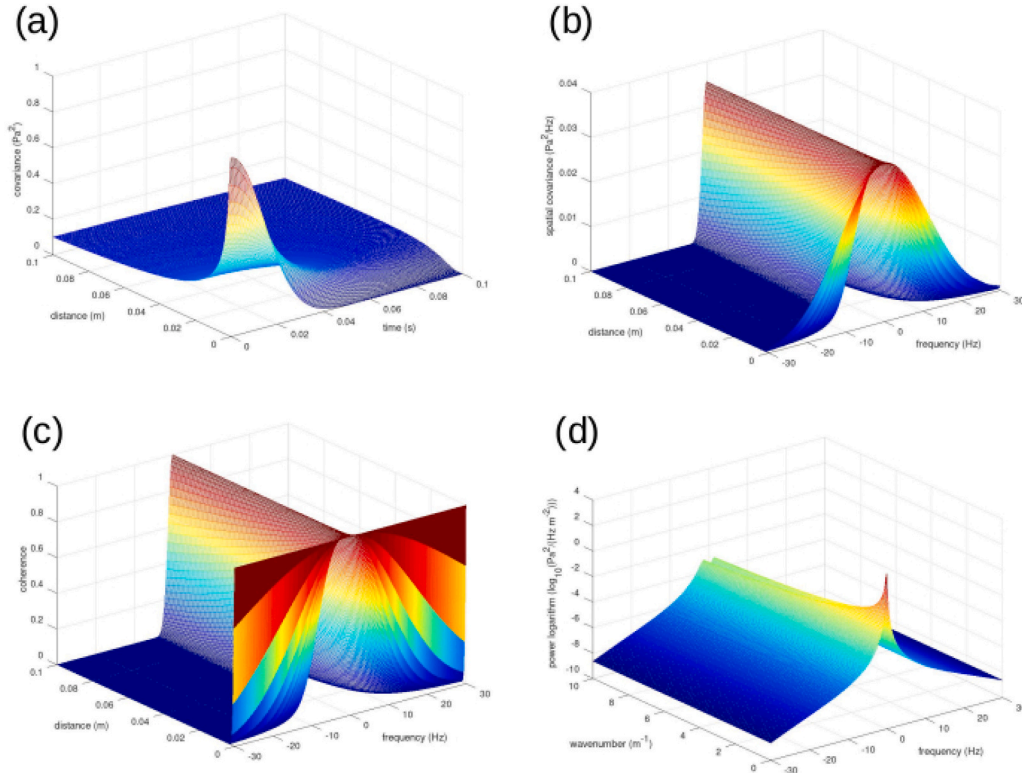


Fig. 2. Force random field characteristics for $B_j = 1 \text{ Pa}^2$, $T_j = 0.01 \text{ s}$ and $R_j = 0.001 \text{ m}$ ($j = x, y, z$): (a) space–time covariance function; (b) spatial covariance function with respect to the frequency; (c) coherence function; (d) power spectral density function (in logarithmic scale). (For interpretation of the references to color in this figure legend, the reader is referred to the Web version of this article.)

covariance function in Eq. (5). Appendix D shows that these extreme values are reached for $r = r_1 \equiv 0$ m, whatever t is, and for $r = r_2 \equiv R_j$.

$\sqrt{\left(\frac{t}{\sqrt{2}T_j}\right)^4 - 1}$, when $t \geq \sqrt{2}T_j$ only. The covariance function undergoes to a bifurcation at $t = \sqrt{2}T_j$: for time-values lesser than this value, the point r_1 is the (sole) maximum for $\mathcal{R}_{Fj}(r, t)$ (which has no minima). For time-values larger than this value, r_1 becomes a point of minimum (the only one) for the covariance function, while the single maximum moves to r_2 . This means that, when the time overtakes the value $\sqrt{2}T_j$, the maximum of the covariance starts to move away from the origin according to

$$r(t) = R_j \cdot \sqrt{\left(\frac{t}{\sqrt{2}T_j}\right)^4 - 1},$$

that is, with speed

$$\dot{r}(t) = \frac{\sqrt{2}R_j}{T_j} \cdot \frac{\left(\frac{t}{\sqrt{2}T_j}\right)^3}{\sqrt{\left(\frac{t}{\sqrt{2}T_j}\right)^4 - 1}}$$

(when $t \gg \sqrt{2}T_j$, this velocity is almost linear with respect to the time). The physical interpretation of this fact deserves further investigations, but the symmetry with respect to the time suggests that the source-stresses act like a spreading wave, which reaches its maximum value in the origin at zero time.

3. Theoretical power spectra for the average continental crust

In order to evaluate effectiveness of the proposed model to capture main characteristics of the ambient vibration wavefield, it has been applied to a very simple stratigraphic profile, constituted by an elastic crustal layer overlying a half-space, both homogeneous and isotropic (Table 1). This profile aims at representing the average seismic structure of the shallowest part of the continental crust: P-wave velocities have been chosen as indicative averages of the values shown in Fig. 2 of Mooney et al. [45]; while values of the S-wave velocities and densities have been deduced from the P-waves profile by following Brocher [46]. Damping values have been set as almost negligible in order to simulate nearly elastic materials (the way in which the viscosity is introduced into the computation is explained in Refs. [36,41]). The covariance function along the three spatial directions is supposed to be the same: the three variances have a common value, $B \equiv B_x = B_y = B_z$, and the three parameter pairs (T_j, R_j) ($j = x, y, z$) are assumed as equal.

Outcomes of this model are expected to simulate average power spectra of the ambient vibrations, whose upper (NHNM, New High-Noise Model) and lower (NLNM, New Low-Noise Model) bounds were determined by Peterson [40]. The two curves NLNM and NHNM relative to the ground-motion displacement in the range [0.01, 10] Hz are plotted in the first panel of Fig. 3 (see also Ref. [47]) along with the power spectra obtained by the present model for three couples of values of (T, R) fulfilling the relationship in Eq. (11). In general, our numerical computations show that parameters for which R/T^2 has the same value give the same power spectra and, that these spectra perfectly adapt to the Peterson's bounds, when this ratio values 10 ms^{-2} . This good

Table 1

Seismic stratigraphy for the average continental upper crust.

$H(\text{m})$	$V_P(\text{m/s})$	$V_S(\text{m/s})$	$\rho(\text{kg/m}^3)$	D_P	D_S
2000	3500	1900	2300	0.0001	0.0001
∞	6000	3500	2700	0.0001	0.0001

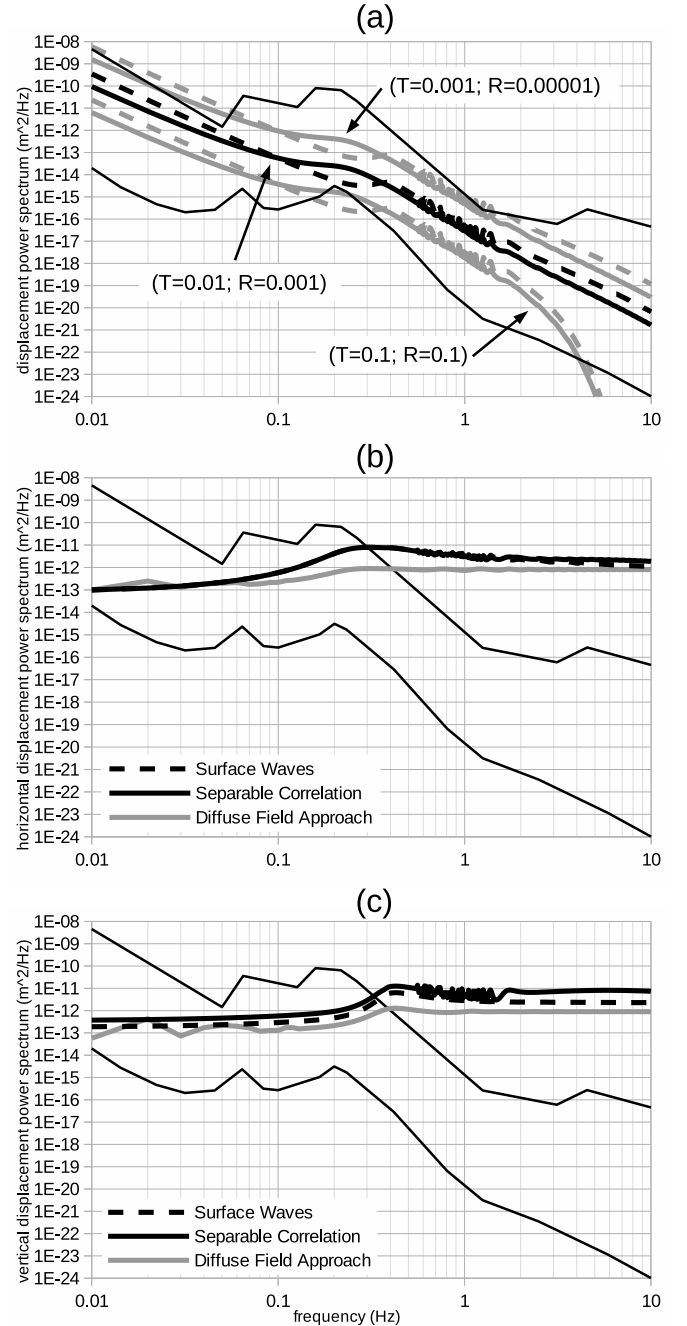


Fig. 3. Comparison of synthetic displacement spectral-power density functions for the stratigraphy in Table 1, with the NLNM (New Low-Noise Model) and NHNM (New High-Noise Model) bounds by Peterson [40] marked by thin black lines. (a) Horizontal (thick continuous lines) and vertical (thick dashed lines) spectral-power density functions given by the present DSS model with three parameter-pair values linked by Eq. (11); different values for the variance B are chosen for the different couples, in order to avoid superposition and to obtain clear plots (this just implies a vertical translation of the curves). (b) Horizontal spectral-power density functions produced by three alternative models (surface-wave approximation, DSS model with separable covariance function and Diffuse Field Approach); B -values are chosen to make the curves coincident at the minimum frequency. (c) Vertical spectral-power density functions produced by the same three alternative models in panel (b); B -values are the same of panel (b).

adaption keeps for smaller values of this ratio, while, when it becomes greater enough than 10 ms^{-2} , the patterns start to depart from the shape marked by the bounds. Moreover, when $T > 0.01 \text{ s}$, whatever R -value is (e.g., when $T = 0.1 \text{ s}$ and $R = 0.1 \text{ m}$), the synthetic pattern remarkably deflects from the Peterson's bounds in the high frequency range. These findings suggest that

$$R \leq (10 \text{ ms}^{-2}) \cdot T^2 \quad \wedge \quad T \leq 0.01 \text{ s}.$$

For the frequency range of interest here, the second bound acceptably fulfils the condition in order that approximate formula in Eq. (10) holds. Moreover, Peterson's bounds also impose a relatively narrow admissible value range for the variance B , depending on the values assumed by the couple (T, R) : e.g., when $T = 0.01 \text{ s}$ and $R = 0.001 \text{ m}$, $\sqrt{B} \in [24; 45] \text{ Pa}$ has to hold.

As a whole, a noticeable physical characterization of the ambient-vibration phenomenon emerges from this analysis: the new proposed DSS model with non-separable covariance in Eq. (6) allows to reproduce the patterns of displacement power spectra when covariance parameters are suitably tuned, without any further assumption. Nothing similar can be obtained by considering the other models (second and third panel in Fig. 3): neither the DSS model with separable covariance (Eq. (4)), nor the DFA model are able to reproduce the decreasing trend of spectral amplitudes. The same is true when the surface-wave approximation is considered. What is intriguing is that these last three models provide the same patterns: this suggests a form of equivalence between the respective underlying assumptions.

4. An experimental case: Mirandola (Northern Italy)

Beyond the possibility to explain the overall spectral configuration of ambient vibrations, the model is requested to reproduce features more interesting for applications, such as, e.g., the HVSF curve. To test this ability, the site of the Mirandola's strong-motion station (belonging to the Italian accelerometric network, RAN), previously examined in Lunedei and Albarello [36,41], is here considered to compare the synthetic outcomes of the present theory with the correspondent experimental ones. Close to this station, an experimental dispersion curve for the vertical ground-motion and some HVSF curves have been obtained from ambient vibration measurements. A cross-hole test was also performed down to 125 m of depth. The simplified profile for P-waves, S-waves and densities is shown in Table 2 [41].

In first panel of Fig. 4, synthetic HVSF curves produced by the DSS models (both with non-separable and separable covariance function), the DFA and the surface-wave approximation for the profile in Table 2 are compared with the experimental one. It clearly emerges that, except as concerns smallest frequencies, DSS and DFA models are equally able to fit (within the experimental uncertainty) the experimental HVSF curve, which is not the case of surface wave approximation. Second and third panel of this figure show the corresponding observed displacement power spectra, together with the ones generated by these theoretical models. Although none of the models is able to perfectly fit experimental power spectra on the entire considered frequency range, the new DSS model shows, unlike the alternative ones, able to catch the main features of the observed patterns: the nearly monotonic decrease of spectral amplitudes with frequency and the *plateaux* around the H/V peak frequency. By posing the variance $\sqrt{B} \in [0.4; 3.2] \text{ Pa}$, this reproduction is, as the diagram shows, quantitative too: very good for higher frequency, just indicative for the lower ones. The lack of fit below few hertz may be due to the shallow depth reached by experimental velocity profile in Table 2 (less than 130 m), which does not allow to account for deeper soil configurations responsible for the low frequency pattern. We highlight, however, that the power spectra simulated by the new DSS model shows the correct behaviour with respect to the frequency. On the other hand, the good fit in the frequency range dominated by anthropic sources might be surprising because these were not considered in the

Table 2

Simplified stratigraphy of the Mirandola's RAN site.

H (m)	V_P (m/s)	V_S (m/s)	ρ (kg/m ³)	D_P	D_S
2	640	170	1500	0.020	0.020
2	770	170	1500	0.015	0.015
2	940	180	1500	0.010	0.010
4	1360	200	1500	0.005	0.005
2	1770	210	2000	0.001	0.001
10	1740	210	2000	0.001	0.001
2	1760	230	2000	0.001	0.001
2	1820	260	2000	0.001	0.001
2	1760	280	2000	0.001	0.001
4	1790	290	2000	0.001	0.001
2	1820	300	2000	0.001	0.001
2	1840	320	2000	0.001	0.001
2	1840	340	2000	0.001	0.001
3	1860	350	2000	0.001	0.001
9	1890	330	2000	0.001	0.001
3	1890	330	2000	0.001	0.001
4	1940	360	2100	0.001	0.001
3	1960	420	2100	0.001	0.001
4	2030	410	2100	0.001	0.001
6	2000	350	2100	0.001	0.001
3	1920	350	2100	0.001	0.001
2	2000	410	2100	0.001	0.001
12	2110	430	2100	0.001	0.001
9	2160	410	2100	0.001	0.001
6	2170	510	2100	0.001	0.001
8	2290	440	2100	0.001	0.001
5	2560	530	2200	0.001	0.001
3	2810	740	2300	0.001	0.001
∞	3170	860	2300	0.001	0.001

model. It is worth to note, however, that the experimental curves in Fig. 4 originate from measurements carried out in a very quiet period, just after a damaging earthquake affecting the area in 2012 (see, e.g., Ref. [48]), with the consequent interruption of industrial and economic activity. We also note that the variance B is here one order of magnitude lower than the one in the previous section. This could be the effect of the local stratigraphy and could be interpreted as a symptom of the energy trapping inside the soft layer stack, which allows a lower source strength to provide relatively larger ground-motion.

5. Conclusions

A new version of the ambient-vibration full-wavefield Distributed Surface Sources (DSS) model is here presented, which generalizes the one described in Lunedei and Albarello [36,41]; by including a frequency dependent spatial correlation among the sources generating ambient vibrations.

The novelty of this assumption goes beyond just introducing a frequency-dependence of the source power spectra, because it consists in making the frequency-dependence as a function of distance. The natural physical interpretation is a link between this dependence and the spatial extension of the sources, which describes an important physical aspect of the ambient-vibration phenomenon. In fact, this allows reproducing, without any additional *ad-hoc* hypothesis, the expected pattern for the average worldwide ambient-vibration power spectral density function in a frequency range of interest for the shallow subsoil exploration and, therefore, for applications both geophysical and engineering. Even though calibrating the model by the sea-wave dynamics may seem a limitation, it can surely be regarded as a first step, because, due to the linearity of the formalization, the contribution of different kinds of uncorrelated sources (i.e., different parametrizations of the source correlation function) to the wavefield can be introduced by simply summing the respective covariance functions. In light of this, nothing hampers the introduction of different kinds of sources, possibly more effective in specific frequency ranges (e.g., above 1 Hz, where anthropic sources may

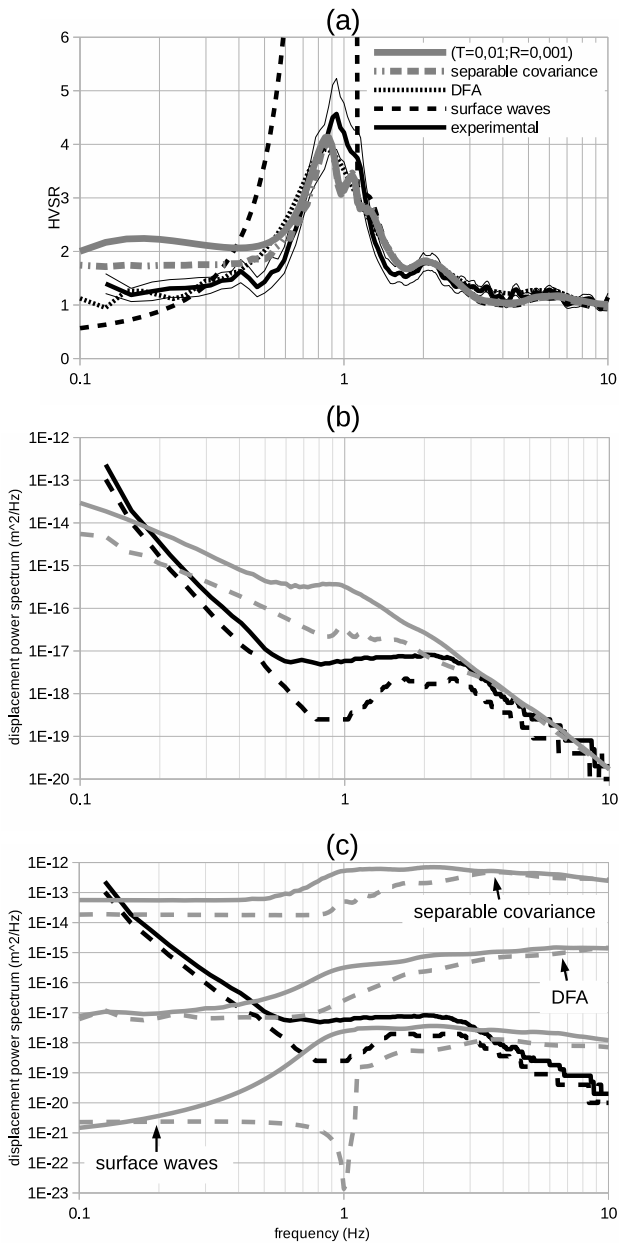


Fig. 4. Comparison of experimental HVSR and displacement power spectra at the Mirandola test site with synthetic curves obtained by different ambient vibration models by considering data in Table 2. Since implementation of damping in the DFA model is different from the one used in our code, no different values can be assigned to different layers, so damping values for the DFA model are equivalent to 0.001 for all the layers. (a) Solid black line: HVSR experimental curve; thin black lines: 95% confidence intervals; gray solid line: outcome of the present model ($T = 0.01$ s and $R = 0.001$ m); dotted dashed gray lines: outcome of the DSS model with separable covariance; dotted black line: outcome of the DFA (Diffuse Field Approach); dashed black line: outcome of the surface-wave approximation. (b) Black lines: experimental spectral power density function of the horizontal (solid) and vertical (dashed) components; gray lines: outcomes of the present model ($T = 0.01$ s and $R = 0.001$ m) for vertical (solid) and horizontal (dashed) components; B -value is chosen in order experimental and theoretical curves are approximately superimposed at higher frequencies. (c) Black lines: experimental spectral power density function of the horizontal (solid) and vertical (dashed) components; gray lines: outcomes of the DSS model with separable covariance, DFA (Diffuse Field Approach) and surface-wave approximation; different values for the variance B are chosen for the different couples, in order to avoid superposition and to obtain clear plots.

play a major role). One could also imagine trial-and-error inversion procedures aiming at fitting observations by defining suitable covariance configurations for sources along with subsoil seismic structure. This also opens the possibility to use on purpose the power spectra of ambient vibration components along with their ratios.

In the case study here considered, the model provides outcomes fully compatible with observed HVSR and, on this regard, is at least as much effective than the DFA in practical applications. Corresponding power spectrum, albeit exhibit (spontaneously) a behaviour coherent with the experimental one, show significant differences at low frequency domain. In order to shed light on this disagreement and check the effectiveness and usefulness of the model, as well as to explore its potentialities, a number of tests in different situations should be carried out. Moreover, further studies are needed in order to reduce numerical instabilities, often occurring, due to the computation of the power integrals (which integrands presents a number of poles), which could be faced following the way proposed by García-Jerez et al. [21] and García-Jerez and Sánchez-Sesma [49] for the DFA, which is the next step to improve our model.

Author statement

Enrico Lunedei: Conceptualization, Methodology, Software, Validation, Investigation, Writing - Original Draft, Writing - Review & Editing.

Dario Albarello: Conceptualization, Investigation, Resources, Writing - Original Draft, Writing - Review & Editing, Supervision, Project administration.

Declaration of competing interest

The authors declare that they have no known competing financial interests or personal relationships that could have appeared to influence the work reported in this paper.

Acknowledgements

E. L. thanks the *Dipartimento di Scienze Fisiche, della Terra e dell'Ambiente* of the University of Siena (Italy), where the first part of this work has been realized when he was working in that place.

This research did not receive any specific grant from funding agencies in the public, commercial, or not-for-profit sectors.

A.

The four hypothesis adopted in Refs. [36,41] are the following ones:

- 1) A linear relationship links the displacement and the force stochastic fields:

$$U_i(x, y, t) = \sum_{j=x,y,z} \int_{\mathbb{R}^3} G_{ij}(\xi, \eta, \tau) \cdot F_j(x - \xi, y - \eta, t - \tau) d\xi d\eta d\tau, \quad (13)$$

for $i = x, y, z$, being G_{ij} the component along the i -th direction of the Green's function, relative to the source-stress component along the j -th direction (this hypothesis derives from the fact that ambient-vibration displacements are assumed to be small).

- 2) Power spectral density functions exist for both the fields, which are represented by the respective spectral matrices,

$$\mathbf{h}_\bullet(k_x, k_y, \omega) =$$

$$= \begin{pmatrix} h_{\bullet,xx}(k_x, k_y, \omega) & h_{\bullet,xy}(k_x, k_y, \omega) & h_{\bullet,xz}(k_x, k_y, \omega) \\ h_{\bullet,yx}(k_x, k_y, \omega) & h_{\bullet,yy}(k_x, k_y, \omega) & h_{\bullet,yz}(k_x, k_y, \omega) \\ h_{\bullet,zx}(k_x, k_y, \omega) & h_{\bullet,zy}(k_x, k_y, \omega) & h_{\bullet,zz}(k_x, k_y, \omega) \end{pmatrix},$$

where “ \bullet ” stands for U or F when the displacement or the force fields are respectively considered. Diagonal and off-diagonal terms respectively represent auto-spectra and cross-spectra of the corresponding field components. All of them depend on the angular frequency ω and on the 2D wavenumber-vector $\mathbf{k} \equiv (k_x, k_y)^T$, corresponding to the time (t) and the horizontal position ($\mathbf{x} \equiv (x, y)^T$), respectively. Due to formula in Eq. (13), one has

$$\mathbf{h}_U(k_x, k_y, \omega) = \hat{\mathbf{G}}(k_x, k_y, \omega) \cdot \mathbf{h}_F(k_x, k_y, \omega) \cdot \hat{\mathbf{G}}^*(k_x, k_y, \omega)$$

(e.g., Refs. [42,43]), where “ $*$ ” stands for the hermitian conjugation and

$$\begin{aligned} \hat{\mathbf{G}}(k_x, k_y, \omega) &= \\ &= \begin{pmatrix} \hat{G}_{xx}(k_x, k_y, \omega) & \hat{G}_{xy}(k_x, k_y, \omega) & \hat{G}_{xz}(k_x, k_y, \omega) \\ \hat{G}_{yx}(k_x, k_y, \omega) & \hat{G}_{yy}(k_x, k_y, \omega) & \hat{G}_{yz}(k_x, k_y, \omega) \\ \hat{G}_{zx}(k_x, k_y, \omega) & \hat{G}_{zy}(k_x, k_y, \omega) & \hat{G}_{zz}(k_x, k_y, \omega) \end{pmatrix}, \end{aligned}$$

is the Green’s matrix in the wavenumber–frequency domain. The entries of this matrix are the Fourier transforms of the corresponding entries of the Green’s matrix in the space–time domain:

$$\hat{G}_{ij}(k_x, k_y, \omega) = \int_{\mathbb{R}^3} G_{ij}(x, y, t) \cdot e^{i(k_x x + k_y y + \omega t)} dx dy dt,$$

for $i, j = x, y, z$.

3) The three Cartesian components of the force field are uncorrelated one another. This implies that all the cross-spectra are zero and the force spectral matrix is diagonal:

$$\begin{aligned} \mathbf{h}_F(k_x, k_y, \omega) &= \\ &= \text{diag}(h_{F,xx}(k_x, k_y, \omega), h_{F,yy}(k_x, k_y, \omega), h_{F,zz}(k_x, k_y, \omega)) \end{aligned}$$

4) Each of the spatial covariances of the three Cartesian components of the force field is isotropic in the horizontal plane.

Under these hypotheses, in the quoted articles the power spectral density functions of the displacement components along the three Cartesian principal directions, as a function of the (angular) frequency ω and of (vectorial) horizontal wavenumber $\mathbf{k} \equiv (k_x, k_y)^T$, are computed. Passing to a polar coordinate system in the wavenumber plane, i.e. $\mathbf{k} \equiv (k, \varphi)^T$, they are

$$h_{U,ii}(k, \varphi, \omega) = \sum_{j=x,y,z} \left| \hat{G}_{ij}(k, \varphi, \omega) \right|^2 \cdot h_{F,ij}(k, \varphi, \omega),$$

for $i = x, y, z$, where

$$\hat{G}_{xx}(k, \varphi, \omega) = -[R_{11}(k, \omega) \cdot \cos^2 \varphi + L_1(k, \omega) \cdot \sin^2 \varphi],$$

$$\hat{G}_{xy}(k, \varphi, \omega) = -[R_{11}(k, \omega) - L_1(k, \omega)] \cdot \cos \varphi \sin \varphi,$$

$$\hat{G}_{xz}(k, \varphi, \omega) = -R_{12}(k, \omega) \cdot \cos \varphi,$$

$$\hat{G}_{yx}(k, \varphi, \omega) = -[R_{11}(k, \omega) - L_1(k, \omega)] \cdot \cos \varphi \sin \varphi,$$

$$\hat{G}_{yy}(k, \varphi, \omega) = -[R_{11}(k, \omega) \cdot \sin^2 \varphi + L_1(k, \omega) \cdot \cos^2 \varphi],$$

$$\hat{G}_{yz}(k, \varphi, \omega) = -R_{12}(k, \omega) \cdot \sin \varphi,$$

$$\hat{G}_{zx}(k, \varphi, \omega) = i \cdot R_{21}(k, \omega) \cdot \cos \varphi,$$

$$\hat{G}_{zy}(k, \varphi, \omega) = i \cdot R_{21}(k, \omega) \cdot \sin \varphi,$$

$$\hat{G}_{zz}(k, \varphi, \omega) = i \cdot R_{22}(k, \omega).$$

Functions L_1 and R_{ij} , which does not depend on φ , are constructed by the propagation matrices in the stratified medium, and they contain all the information about the mechanical properties of the subsoil. Their expressions can be found in Appendix A of Lunedei and Albarello [34]; where in the

formula defining L_H (penultimate equation in left side of p. 1106) the denominator $F_L(k)$ is wanting because of a misprint. These function are similar to the coefficients H and V in Hisada [50]; from which they differ for a factor k and some constants. In Lunedei and Albarello [36,41], explicit formulae for the power spectral density functions of the displacement components along the three Cartesian principal directions are given as

$$\begin{aligned}
 h_{U,xx}(k, \varphi, \omega) &= h_{F,xx}(k, \omega) \cdot [|R_{11}(k, \omega)|^2 \cdot \cos^4 \varphi + |L_1(k, \omega)|^2 \cdot \sin^4 \varphi] + \\
 &+ \left\{ h_{F,xx}(k, \omega) \cdot 2 \cdot \Re \left[R_{11}(k, \omega) \cdot \overline{L_1(k, \omega)} \right] + h_{F,yy}(k, \omega) \cdot |R_{11}(k, \omega) - L_1(k, \omega)|^2 \right\} \cdot \cos^2 \varphi \sin^2 \varphi + \\
 &+ h_{F,zz}(k, \omega) \cdot |R_{12}(k, \omega)|^2 \cdot \cos^2 \varphi; \\
 h_{U,yy}(k, \varphi, \omega) &= h_{F,yy}(k, \omega) \cdot [|R_{11}(k, \omega)|^2 \cdot \sin^4 \varphi + |L_1(k, \omega)|^2 \cdot \cos^4 \varphi] + \\
 &+ \left\{ h_{F,yy}(k, \omega) \cdot 2 \cdot \Re \left[R_{11}(k, \omega) \cdot \overline{L_1(k, \omega)} \right] + h_{F,xx}(k, \omega) \cdot |R_{11}(k, \omega) - L_1(k, \omega)|^2 \right\} \cdot \cos^2 \varphi \sin^2 \varphi + \\
 &+ h_{F,zz}(k, \omega) \cdot |R_{12}(k, \omega)|^2 \cdot \sin^2 \varphi; \\
 h_{U,zz}(k, \varphi, \omega) &= |R_{21}(k, \omega)|^2 \cdot [h_{F,xx}(k, \omega) \cdot \cos^2 \varphi + h_{F,yy}(k, \omega) \cdot \sin^2 \varphi] + |R_{22}(k, \omega)|^2 \cdot h_{F,zz}(k, \omega),
 \end{aligned}$$

which just depend on the modulus of \mathbf{k} and on the angular frequency ω , as a consequence of the hypothesis of isotropy.

B.

Derivation of the formula in Eq. (6). By using Eq. (17.23(13)) of Gradshteyn & Ryzhik [51] or Eq. (11), p. 15, vol. 1 of Bateman [52]; the time Fourier-transform of the correlation in Eq. (5) is

$$\begin{aligned}
 C_{F,j}(r; \omega) &= \int_{-\infty}^{+\infty} \mathcal{R}_{F,j}(r, t) \cdot e^{-i\omega t} dt = \\
 &= \frac{B_j}{\left[\left(\frac{r}{R_j} \right)^2 + 1 \right]^{1/4}} \cdot \int_{-\infty}^{+\infty} \exp \left\{ - \frac{t^2}{\left\{ 2T_j \left[\left(\frac{r}{R_j} \right)^2 + 1 \right] \right\}^2} \right\} \cdot e^{-i\omega t} dt = \\
 &= \frac{\sqrt{2\pi} B_j}{\left[\left(\frac{r}{R_j} \right)^2 + 1 \right]^{1/4}} \cdot \left\{ \frac{\sqrt{2}}{2T_j \left[\left(\frac{r}{R_j} \right)^2 + 1 \right]^{1/4}} \right\}^{-1} \cdot \exp \left\{ - \omega^2 \cdot \left[\frac{4}{4T_j^2 \sqrt{\left(\frac{r}{R_j} \right)^2 + 1}} \right]^{-1} \right\} = \\
 &= 2\sqrt{\pi} B_j T_j \cdot \exp \left\{ - (\omega T_j)^2 \sqrt{\left(\frac{r}{R_j} \right)^2 + 1} \right\}, \quad j = x, y, z.
 \end{aligned}$$

Derivation of the formula in Eq. (8). The “effective” correlation radius in Eq. (8) is defined as the distance at which the force-field coherence in Eq. (7) has an established value $\gamma \in]0, 1$, that is, for each $j = x, y, z$, the one that fulfils the equation

$$-(\omega T_j)^2 \cdot \left[\sqrt{\left(\frac{r_{\gamma,j}(\omega)}{R_j} \right)^2 + 1} - 1 \right] = \log \gamma \Leftrightarrow$$

$$\sqrt{\left(\frac{r_{\gamma,j}(\omega)}{R_j} \right)^2 + 1} = \frac{\log \gamma}{(\omega T_j)^2} + 1 \Leftrightarrow$$

$$\left(\frac{r_{\gamma,j}(\omega)}{R_j} \right)^2 = \left[\frac{|\log \gamma|}{(\omega T_j)^2} + 1 \right]^2 - 1 = \frac{|\log \gamma|^2}{(\omega T_j)^4} + 2 \frac{|\log \gamma|}{(\omega T_j)^2} \Leftrightarrow$$

$$r_{\gamma,j}(\omega) = \frac{R_j \cdot \sqrt{|\log \gamma|}}{\omega T_j} \cdot \sqrt{\frac{|\log \gamma|}{(\omega T_j)^2} + 2} = \frac{R_j \cdot \sqrt{|\log \gamma|}}{(\omega T_j)^2} \cdot \sqrt{|\log \gamma| + 2(\omega T_j)^2} =$$

$$= \frac{R_j \cdot |\log \gamma|}{(\omega T_j)^2} \cdot \sqrt{1 + 2 \frac{(\omega T_j)^2}{|\log \gamma|}}.$$

Derivation of the formula in Eq. (12). By using Eq. (23) at page 9 of the volume 2 of [52]; the two-dimensional Fourier transform of C_{Fj} in Eq. (6) with respect to the spatial variables, is

$$\begin{aligned}
 h_{F,jj}(k, \omega) &= 2\pi \cdot \int_0^{+\infty} C_{Fj}(r; \omega) \cdot J_0(kr) \cdot r dr = \\
 &= \frac{4\pi\sqrt{\pi}B_jT_j}{\sqrt{r}k} \cdot \int_0^{+\infty} \sqrt{r} \cdot \exp\left\{-\frac{(\omega T_j)^2}{R_j} \cdot \sqrt{r^2 + R_j^2}\right\} \cdot J_0(kr) \cdot \sqrt{kr} dr = \\
 &= \frac{4\pi\sqrt{\pi}B_jT_j}{\sqrt{r}k} \cdot \frac{(\omega T_j)^2}{R_j} \sqrt{k} \left[k^2 + \frac{(\omega T_j)^4}{R_j^2}\right]^{-\frac{3}{2}} \cdot \exp\left\{-R_j \sqrt{k^2 + \frac{(\omega T_j)^4}{R_j^2}}\right\} \cdot \left[1 + R_j \sqrt{k^2 + \frac{(\omega T_j)^4}{R_j^2}}\right] = \\
 &= \frac{4\pi\sqrt{\pi}B_jT_j(\omega T_j)^2}{R_j} \cdot \frac{R_j^3}{[(kR_j)^2 + (\omega T_j)^4]^{\frac{3}{2}}} \cdot \left[1 + \sqrt{(kR_j)^2 + (\omega T_j)^4}\right] \cdot \exp\left\{-\sqrt{(kR_j)^2 + (\omega T_j)^4}\right\} = \\
 &= \frac{\pi^{\frac{3}{2}} \cdot B_j T_j \cdot (2\omega T_j R_j)^2}{\left[\sqrt{(kR_j)^2 + (\omega T_j)^4}\right]^3} \cdot \left[1 + \sqrt{(kR_j)^2 + (\omega T_j)^4}\right] \cdot \exp\left\{-\sqrt{(kR_j)^2 + (\omega T_j)^4}\right\}, \quad j = x, y, z.
 \end{aligned}$$

C.

According to its definition (Appendix A), the space-time Fourier transform of the Green function $\widehat{G}_{ij}(k, \varphi, \omega)$, in the *Système International d'unités* (SI), is expressed in m/Pa; thus, the Green function $G_{ij}(x, y, t)$ is expressed as (m/Pa)/(m²·s). As the displacement $U(x, y, t)$ is measured in m, Eq. (13) implies that the measure unit for $F(x, y, t)$ is Pa. As a consequence, the covariances $\mathcal{R}_{Fj}(r, t)$ and the variances B_j are in Pa². This rectifies what erroneously written in Lunedei and Albarello [36,41] about these units (in particular, b_j of the separable covariance is measured in (Pa·m)²).

D.

The positions of the extreme values of the covariance in Eq. (5) are included among the radius values that make zero the derivative of the covariance function with respect to r

$$\frac{\partial \mathcal{R}_{Fj}(r, t)}{\partial r} = \frac{-B_j \cdot r}{2R_j^2 \cdot \left[\left(\frac{r}{R_j}\right)^2 + 1\right]^{5/4}} \cdot \exp\left\{-\frac{\left(\frac{t}{T_j}\right)^2}{4\sqrt{\left(\frac{r}{R_j}\right)^2 + 1}}\right\} \cdot \left\{1 - \frac{\left(\frac{t}{T_j}\right)^2}{2\left[\left(\frac{r}{R_j}\right)^2 + 1\right]^{1/2}}\right\}$$

The solutions of the equation $\partial \mathcal{R}_{Fj}(r, t)/\partial r = 0$ are just two:

$$r = 0 \quad \vee \quad \frac{\left(\frac{t}{T_j}\right)^2}{2\left[\left(\frac{r}{R_j}\right)^2 + 1\right]^{1/2}} = 1.$$

The first solution always exists, while the second becomes

$$\left[\left(\frac{r}{R_j}\right)^2 + 1\right]^{1/2} = \left(\frac{t}{\sqrt{2} \cdot T_j}\right)^2 \quad \Rightarrow \quad \left(\frac{r}{R_j}\right)^2 = \left(\frac{t}{\sqrt{2} \cdot T_j}\right)^4 - 1,$$

which is, in effect, a solution if and only if

$$\left(\frac{t}{\sqrt{2} \cdot T_j}\right)^4 - 1 \geq 0 \quad \Leftrightarrow \quad t \geq \sqrt{2} \cdot T_j.$$

Then, the two extreme values of the covariance are reached when the point distance r assumes one of this values

$$\begin{cases} r_1 = 0 & , \forall t \\ r_2 = R_j \cdot \sqrt{\left(\frac{t}{\sqrt{2} \cdot T_j}\right)^4 - 1} & , \forall t \geq \sqrt{2} \cdot T_j \end{cases}$$

($r_2 = r_1$ when $t = \sqrt{2} \cdot T_j$). By substituting in Eq. (5),

$$\begin{aligned}\mathcal{R}_{Fj}(r_1, t) &= B_j \cdot \exp \left\{ - \left(\frac{t}{T_j} \right)^2 \right\}, \\ \mathcal{R}_{Fj}(r_2, t) &= \frac{B_j}{\left[\left(\frac{t}{\sqrt{2} \cdot T_j} \right)^4 \right]^{1/4}} \exp \left\{ - \frac{\left(\frac{t}{T_j} \right)^2}{4 \cdot \left(\frac{t}{\sqrt{2} \cdot T_j} \right)^4} \right\} = \\ &= \frac{B_j}{\sqrt{2} \cdot T_j} \exp \left\{ - \frac{\left(\frac{t}{T_j} \right)^2}{4 \cdot \left(\frac{t}{\sqrt{2} \cdot T_j} \right)^2} \right\} = \frac{B_j}{\sqrt{2} \cdot T_j} \cdot e^{-\frac{1}{2}}.\end{aligned}$$

When r_2 exists, it is not difficult to show that $\mathcal{R}_{Fj}(r_2, t) \geq \mathcal{R}_{Fj}(r_1, t)$, so the maximum of the covariance function correspond to the distance r_2 .

References

- Nakamura Y. A method for dynamic characteristics estimation of subsurface using microtremors on the ground surface. *Q Rep Railway Tech Res Inst* 1989;30:25–33.
- Tokimatsu K, Ishihara K. Geotechnical site characterization using surface waves. In: *Earthquake geotechnical engineering: proceedings of IS-Tokyo '95, the first International Conference on earthquake Geotechnical engineering*, Tokyo, 14–16 november, 1995. vol. 3. Rotterdam: A.A. Balkema Publishers; 1997. p. 1333–68.
- Bard PY. Microtremor measurements: a tool for site effect estimation?. In: *Proceedings of the 2nd Int. Symposium on the Effects of Surface Geology on Seismic Motion*, Yokohama, Japan. 3; 1998. p. 1251–79.
- Molnar S, Cassidy JF, Castellaro S, Cornou C, Crow H, Hunter JA, Matsushima S, Sánchez-Sesma FJ, Yong A. Application of microtremor horizontal-to-vertical spectral ratio (MHVSR) analysis for site characterization: state of the art. *Surv Geophys* 2018;39:613–31. <https://doi.org/10.1007/s10712-018-9464-4>.
- Aki K. Space and time spectra of stationary stochastic waves, with special reference to microtremors. *Bull Earthq Res Inst* 1957;35:415–56.
- Okada H. The microtremor survey method, *Gephys. Monogr. Series*, vol. 12. Society of Exploration Geophysicists; 2003. p. 135.
- Asten MW, Hayashi K. Application of the spatial auto-correlation method for shear-wave velocity studies using ambient noise. *Surv Geophys* 2018;39:633–59. <https://doi.org/10.1007/s10712-018-9474-2>.
- Albarello D, Baliva F. 382. In: Mucciarelli Marco, Herak Marijan, Cassidy John, editors. *In-situ estimates of material damping from environmental noise measurements. Increasing seismic safety by combining engineering technologies and seismological data (NATO science for peace and security series C: environmental)*, vol. XVIII. Springer; 2009, ISBN 978-1-4020-9194-0. p. 73–84.
- Parolai S. Shear wave quality factor Q_s profiling using seismic noise data from microarrays. *J Seismol* 2014;18:695–704. <https://doi.org/10.1007/s10950-014-9440-5>.
- Foti S, Parolai S, Albarello D, Picozzi M. Application of surface-wave methods for seismic site characterization. *Surv Geophys* 2011;32:777–825.
- Arai H, Tokimatsu K. Effect of Rayleigh and Love waves on microtremor H/V spectra. In: *Proceedings of the 12th world Conferences on earthquake engineering (WCEE)*, Auckland, New Zealand; 2000. <http://www.nicee.org/wcee/>.
- Arai H, Tokimatsu K. S-wave velocity profiling by inversion of microtremor H/V spectrum. *Bull Seismol Soc Am* 2005;95(5):1766–78.
- Lunedei E, Malischewsky P. A review and some new issues on the theory of the H/V technique for ambient vibrations. In: Ansal A, editor. *Theme lecture at the second European Conference on earthquake engineering and seismology (2ECEEES)*, Istanbul (Turkey), 24–29 august 2014. *Perspectives on European earthquake engineering and seismology - volume 2*; 2014. Springer International Publishing ed. [ISBN: 978-3-319-16963-7 (printed) 978-3-319-16964-4 (electronic)], pp. 371–394, doi:10.1007/978-3-319-16964-4, free access on, <http://link.springer.com/book/10.1007%2F978-3-319-16964-4>.
- Bonnefoy-Claudet S, Cotton F, Bard PY. The nature of noise wavefield and its applications for site effects studies: a literature review. *Earth Sci Rev* 2006;79(7):205–27.
- Bonnefoy-Claudet S, Köhler A, Cornou C, Wathelet M, Bard PY. Effects of Love waves on microtremor H/V ratio. *Bull Seismol Soc Am* 2008;98(1):288–300. <https://doi.org/10.1785/0120070063>.
- Albarello D, Lunedei E. Structure of ambient vibration wavefield in the frequency range of engineering interest ([0.5,20] Hz): insights from numerical modelling. *Near Surf Geophys* 2011;9:543–59. <https://doi.org/10.3997/1873-0604.2011017>.
- Fäh D, Kind F, Giardini D. A theoretical investigation of average H/V ratios. *Geophys J Int* 2001;145:535–49.
- Herak M. ModelHVSR – a Matlab tool to model horizontal-to-vertical spectral ratio of ambient noise. *Comput Geosci* 2008;34(11):1514–26. <https://doi.org/10.1016/j.cageo.2007.07.009>.
- Lunedei E, Albarello D. On the seismic noise wave field in a weakly dissipative layered Earth. *Geophys J Int* 2009;177(3):1001–14. 10.1111/j.1365-246X.2008.04062.x (Erratum doi:10.1111/j.1365-246X.2009.04344.x).
- Sánchez-Sesma FJ, Rodríguez M, Iturrarán-Viveros U, Luzón F, Campillo M, Margerin L, García-Jerez A, Suarez M, Santoyo MA, Rodríguez- Castellanos A. A theory for microtremor H/V spectral ratio: application for a layered medium. *Geophys J Int* 2011;186:221–5. <https://doi.org/10.1111/j.1365-246X.2011.05064.x>.
- García-Jerez A, Luzón F, Sánchez-Sesma FJ, Lunedei E, Albarello D, Santoyo MA, Almendros J. Diffuse elastic wavefield within a simple crustal model. Some consequences for low and high frequencies. *J Geophys Res: Solid Earth* 2013;118:1–19. <https://doi.org/10.1002/2013JB010107>.
- García-Jerez A, Piña-Flores J, Sánchez-Sesma FJ, Luzón F, Perton M. A computer code for forward computation and inversion of the H/V spectral ratio under the diffuse field assumption. *Comput Geosci* 2016;97:67–78.
- Matsushima S, Kosaka H, Kawase H. Directionally dependent horizontal-to-vertical spectral ratios of microtremors at Onahama, Fukushima, Japan. *Earth Planets Space* 2017;69:96. <https://doi.org/10.1186/s40623-017-0680-9>.
- Spica Z, Perton M, Nakata N, Liu X, Beroza GC. Shallow V_s imaging of the groningen area from joint inversion of multimode surface waves and H/V spectral ratios. *Seismol Res Lett* 2018;89(5):1720–9. <https://doi.org/10.1785/0220180060>.
- Spica ZJ, Perton M, Martin ER, Beroza GC, Biondi B. Urban seismic site characterization by fiber-optic seismology. *J Geophys Res: Solid Earth* 2020;125:e2019JB018656. <https://doi.org/10.1029/2019JB018656>.
- Perton M, Spica ZJ, Clayton RW, Beroza GC. Shear wave structure of a transect of the Los Angeles basin from multimode surface waves and H/V spectral ratio analysis. *Geophys J Int* 2020;220(1):415–27. <https://doi.org/10.1093/gji/ggz458>.
- Lontsi AM, García-Jerez A, Molina-Villegas JC, Sánchez-Sesma FJ, Molkenhuth C, Ohrnberger M, Kruger F, Wang R, Fäh D. A generalized theory for full microtremor horizontal-to-vertical [H/V(z,f)] spectral ratio interpretation in offshore and onshore environments. *Geophys J Int* 2019;218:1276–97. <https://doi.org/10.1093/gji/ggz223>.
- Paolucci E, Albarello D, D'Amico S, Lunedei E, Martelli L, Mucciarelli M, Pileggi D. A large scale ambient vibration survey in the area damaged by May-June 2012 seismic sequence in Emilia-Romagna. Italy. *Bull. Earthq.Eng.* 2015;13(11):3187–206. <https://doi.org/10.1007/s10518-015-9767-5>.
- Tanimoto T, Ishimaru S, Alviuzi C. Seasonality in particle motion of microseisms. *Geophys J Int* 2006;166:253–66.
- Henstridge JD. A signal processing method for circular arrays. *Geophysics* 1979;44(2):179–84.
- Cho I, Tada T, Shinozaki Y. A generic formulation for microtremor exploration methods using three-component records from a circular array. *Geophys J Int* 2006;165(1):236–58. <https://doi.org/10.1111/j.1365-246X.2006.02880.x>.
- Field E, Jacob K. The theoretical response of sedimentary layers to ambient seismic noise. *Geophys Res Lett* 1993;20(24):2925–8.
- Bonnefoy-Claudet S, Cornou C, Bard PY, Cotton F, Moczo P, Kristek J, Fäh D. H/V ratio: a tool for site effects evaluation. Results from 1-D noise simulation. *Geophys J Int* 2006;167:827–37. <https://doi.org/10.1111/j.1365-246X.2006.03154.x>.
- Lunedei E, Albarello D. Theoretical HVSR from the full wave field modelling of ambient vibrations in a weakly dissipative layered Earth. *Geophys J Int* 2010;181:1093–108. <https://doi.org/10.1111/j.1365-246X.2010.04560.x>.
- Ardhuin F, Gualtieri L, Stutzman E. Physics of ambient noise generation by ocean waves. In: Nakata N, Gualtieri L, Fichtner A, editors. *Seismic ambient noise*. UK: Cambridge Univ.Press.; 2019, ISBN 978-1-108-41708-2. p. 69–104.

- [36] Lunedei E, Albarello D. Horizontal-to-vertical spectral ratios from a full-wavefield model of ambient vibrations generated by a distribution of spatially correlated surface sources. *Geophys J Int* 2015;201:1140–53. <https://doi.org/10.1093/gji/ggv046>.
- [37] Apel JR. *Principles of ocean physics*. Acad.Press; 1987. p. 631.
- [38] Tanimoto T. Excitation of normal modes by atmospheric turbulence: source of long period seismic noise. *Geophys J Int* 1999;136:345–402.
- [39] Webb SC. The Earth's hum: the excitation of Earth normal modes by ocean waves. *Geophys J Int* 2008;174:542–66. <https://doi.org/10.1111/j.1365-246X.2008.03801.x>.
- [40] Peterson JR. Observations and modeling of seismic background noise. U.S. Geol. Surv. Tech. Rept., Open-File Report 1993;93–322:94. <https://doi.org/10.3133/ofr93322>.
- [41] Lunedei E, Albarello D. Power spectral density function and spatial autocorrelation of the ambient vibration full-wavefield generated by a distribution of spatially correlated surface sources. *Geophys J Int* 2016;204:1817–37. <https://doi.org/10.1093/gji/ggv559>.
- [42] Priestley MB. *Spectral analysis and time series*. London, Great Britain: Academic Press; 1981.
- [43] Vanmarcke E. *Random fields – analysis and synthesis (revised and expanded. new edition)*. Singapore: World Scientific Publishing; 2010.
- [44] Christakos G. *Random field models in Earth sciences*. Acad.Press; 1992. p. 474.
- [45] Mooney WD, Prodehl C, Pavlenkova NI. Seismic velocity structure of the continental lithosphere from controlled source data. *Int Geophys* 2002;81(A): 887–910. [https://doi.org/10.1016/S0074-6142\(02\)80261-3](https://doi.org/10.1016/S0074-6142(02)80261-3).
- [46] Brocher TM. Empirical relations between elastic wavespeeds and density in the Earth's crust. *Bull Seismol Soc Am* 2005;95(6):2081–92. <https://doi.org/10.1785/0120050077>.
- [47] Bormann P. Conversion and comparability of data presentations on seismic background noise. *JSeismol* 1998;2:37–45.
- [48] Carannante S, Argnanì A, Massa M, D'Alema E, Lovati S, Moretti M, Cattaneo M, Augliera P. The May 20 (MW 6.1) and 29 (MW 6.0), 2012, Emilia (Po Plain, northern Italy) earthquakes: new seismotectonic implications from subsurface geology and high-quality hypocenter location. *Tectonophysics* 2015;655:107–23. <https://doi.org/10.1016/j.tecto.2015.05.015>.
- [49] García-Jerez A, Sánchez-Sesma FJ. Slowly-attenuating P-SV leaky waves in a layered elastic halfspace. Effects on the coherences of diffuse wavefields. *Wave Motion* 2015;54:43–57. <https://doi.org/10.1016/j.wavemoti.2014.11.010>.
- [50] Hisada Y. An efficient method for computing Green's functions for a layered half-space with sources and receivers at close depths. *Bull Seismol Soc Am* 1994;84(5): 1456–72.
- [51] Gradshteyn IS, Ryzhik IM. *Table of integrals, series, and products*. VI edition. USA: Academic press; 2000.
- [52] Bateman H. *Tables of integral transforms, volumes I & II*. New York: McGraw-Hill Book Company; 1954. <http://resolver.caltech.edu/CaltechAUTHORS:20140123-101456353>. 07-019549-8.
- [53] Lanchet C, Bard PY. Numerical and theoretical investigations on the possibilities and limitations of Nakamura's technique. *J. Phys. Earth* 1994;42:377–97.